Lawrence Berkeley National Laboratory
Materials Sciences

Authors
Paulsen, Joseph D
Hohlfeld, Evan
King, Hunter
et al.

Curvature-induced stiffness and the spatial variation of wavelength in wrinkled sheets

Joseph D. Paulsen[a,b,1], Evan Hohlfeld[a,1], Hunter King[a], Jiangshui Huang[a,b], Zhanlong Qiu[a], Thomas P. Russell[b], Narayanan Menon[a,2], Dominic Vella[c,2], and Benny Davidovitch[a,2]

[a]Department of Physics, University of Massachusetts, Amherst, MA 01003; [b]Department of Polymer Science and Engineering, University of Massachusetts, Amherst, MA 01003; and [c]Mathematical Institute, University of Oxford, Oxford OX2 6GG, United Kingdom

Wrinkle patterns in compressed thin sheets are ubiquitous in nature and technology, from the furrows on our foreheads to crinkly plant leaves, from ripples on plastic-wrapped objects to the protein film on milk. The current understanding of an elementary descriptor of wrinkles—their wavelength—is restricted to deformations that are parallel, spatially uniform, and nearly planar. However, most naturally occurring wrinkles do not satisfy these stipulations. Here we present a scheme that quantitatively explains the wrinkle wavelength beyond such idealized situations. We propose a local law that incorporates both mechanical and geometrical effects on the spatial variation of wrinkle wavelength. Our experiments on thin polymer films provide strong evidence for its validity. Understanding how wavelength depends on the properties of the sheet and the underlying liquid or elastic subphase is crucial for applications where wrinkles are used to sculpt surface topography, to measure properties of the sheet, or to infer forces applied to a film.

elastic sheets | wrinkles | curved topography

Wrinkles emerge in response to confinement, allowing a thin sheet to avoid the high energy cost associated with compressing a fraction $\tilde{\Delta}$ of its length (Fig. 1) (1–7). The wavelength, λ, of wrinkles reflects a balance between two competing effects: the bending resistance, which favors large wavelengths, and a restoring force that favors small amplitudes of deviation from the flat, unwrinkled state. Two such restoring forces are those due to the stiffness of a solid foundation or the hydrostatic pressure of a liquid subphase (Fig. 1A). Cerda and Mahadevan (1) realized that a tension in the sheet can give rise to a qualitatively similar effect (Fig. 1B) and thereby proposed a universal law that applies in situations where the wrinkled sheet is nearly planar and subjected to uniaxial loading:

$$\lambda = 2\pi (B/K_{\text{eff}})^{1/4}. \qquad [1]$$

Here the bending modulus $B = Et^3/[12(1 - \Lambda^2)]$ (with E the Young's modulus, t the sheet's thickness, and Λ the Poisson ratio), whereas out-of-plane deformation is resisted by an effective stiffness, K_{eff}, which can originate from a fluid or elastic substrate, an applied tension, or both. Eq. 1 is appealing in its simplicity, but it applies only for patterns that are effectively one-dimensional. In particular, it does not apply when the stress varies spatially or when there is significant curvature along the wrinkles.

Here, we study two experimental settings in which these limitations are crucial: (*i*) indentation of a thin polymer sheet floating on a liquid, which leads to a horn-shaped surface with negative Gaussian curvature, and (*ii*) a circular sheet attached to a curved liquid meniscus with positive Gaussian curvature. In both cases, wrinkle patterns live on a curved surface, show spatially varying wavelengths, and are limited in spatial extent. The extent of finite wrinkle patterns in a variety of such 2D situations has recently been addressed (6, 8–11) and was found to depend largely on external forces and boundary conditions. However, a general prescription for the internal structure of the pattern (i.e., the wavelength and any spatial dependence) has been lacking.

Our work leads to two central insights: that the curvature of the subphase gives rise to a new stiffness of geometric origin (which dominates K_{eff} here) and that a local version of the universal law [1] is sufficient to describe the spatial variation of wrinkle wavelengths. These insights allow us to implement the law [1] for a spatially varying $\lambda(x)$ by writing

$$K_{\text{eff}}(x) = K_{\text{sub}} + \sigma_{||}(x)[\Phi'(x)/\Phi(x)]^2 + YR_{||}(x)^{-2}, \qquad [2]$$

where K_{sub} is the substrate's stiffness (e.g., $K_{\text{sub}} = \rho g$ for a liquid subphase), $\sigma_{||}(x)$ and $R_{||}(x)$ are, respectively, the tensile stress and radius of curvature along the wrinkles, $Y = Et$ is the stretching modulus of the sheet, and $\Phi(x)^2$ is proportional to the fractional length $\tilde{\Delta}$ absorbed by the wrinkles. The use of [2] together with [1], which we call the "local λ law," greatly expands the quantitative description of wrinkle patterns.

Theory

We derive the local λ law in Eqs. 1 and 2 by considering the setup depicted in Fig. 1C: a rectangular sheet of thickness t and length L attached to a deformable, cylindrical substrate of radius R. Although this idealized system is not studied here experimentally (and a real cylinder may not actually buckle in the orderly way shown in Fig. 1C), it provides a simple, pedagogic framework in which to consider the various types of stiffnesses that govern the wrinkle wavelength.

For simplicity, we assume the Winkler model, where the substrate responds linearly to a deflection from its rest shape, and use the Föppl–von Kármán (FvK) equations for the mechanical equilibrium of the sheet. Here the sheet can be described using planar coordinates $(x \approx R\theta, y)$ with the y axis parallel to the
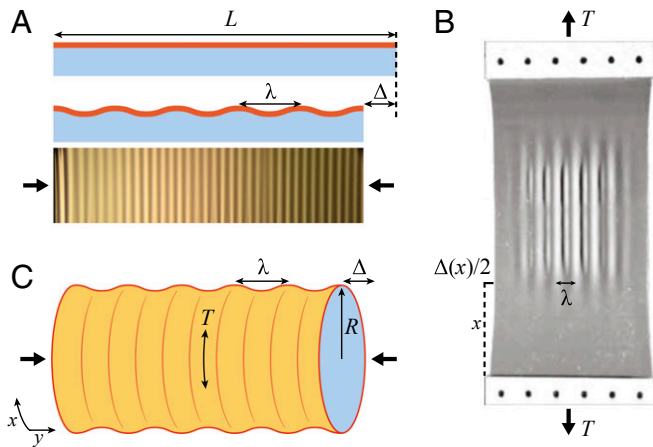
Fig. 1. Parallel wrinkles with three different sources of substrate stiffness: (*A*) elastic or gravitational forces, (*B*) tensile stresses, or (*C*) curvature. The examples shown are for (*A*) unaxial compression of a floating sheet (e.g., from ref. 27), (*B*) a rectangular sheet that is clamped along two edges and stretched, and (*C*) the cylindrical setup discussed in *Theory*. In all examples, a fraction $\widetilde{\Delta} = \Delta/L$ of the sheet's length in the confined direction is absorbed by wrinkles. *B* is reprinted with permission from ref. 33.

cylinder axis. The shape of the sheet $\zeta(x,y)$ is determined by the normal force balance (first FvK equation)

$$B\nabla^4 \zeta - \sigma_{xx}\frac{\partial^2 \zeta}{\partial x^2} - \sigma_{yy}\frac{\partial^2 \zeta}{\partial y^2} + K_{\text{sub}}\left[\zeta - \zeta_{\text{cyl}}(x)\right] = 0. \qquad [3]$$

In the absence of boundary loads, there is no in-plane stress in the sheet ($\sigma_{xx} = \sigma_{yy} = 0$). If the sheet is sufficiently thin or the subphase is sufficiently stiff (large K_{sub}), the sheet will wrap the substrate, $\zeta(x,y) = \zeta_0(x)$, where $\zeta_0(x)$ is close to the cylindrical, undeformed shape of the substrate, $\zeta_{\text{cyl}}(x)$.

Now consider the effect of a compression along the cylinder axis ($\mathbf{e}_y$) and/or a tension T in the azimuthal direction ($\mathbf{e}_x$). These will bring the sheet edges at ($y = \pm L/2$) together by an amount $\Delta(x)$. A sufficiently thin sheet will avoid compression by buckling out of plane; we assume for the following discussion that the sheet forms wrinkles of wavelength λ in the y direction about $\zeta_0(x)$ that accommodate the excess length $\Delta(x)$. A natural ansatz for the shape is then

$$\zeta(x,y) = \zeta_0(x) + f(x)\cos(2\pi y/\lambda). \qquad [4]$$

The amplitude of the wrinkles must exactly accommodate the excess length $\Delta(x)$. This "slaving condition" implies

$$f(x)/\lambda \equiv \Phi(x) \approx \sqrt{\widetilde{\Delta}(x)}\Big/\pi, \qquad [5]$$

where $\widetilde{\Delta}(x) = \Delta(x)/L$. Note that f/λ remains fixed as the sheet thickness $t \to 0$ (such that the excess length is properly accommodated), even though f and λ vanish individually.

The formation of wrinkles enables a complete relaxation of compressive and shear stresses. As $t \to 0$, the stress field approaches the "tension-field" limit (12, 13) [also known as the "membrane" (13) or "relaxed energy" (14, 15) limit] so that

$$\sigma_{xx} \to \sigma_{xx}^{(0)} \approx T, \quad \sigma_{xy}, \sigma_{yy} \to 0. \qquad [6]$$

In the limit of highly bendable sheets ($t \to 0$), the tensile component of the stress [6] remains finite (in an expansion of the FvK equations in powers of the wrinkle amplitude, f, subjected to the

slaving condition [5]), as does the mean profile of the sheet, $\zeta_0(x)$; these are the leading-order results of the far-from-threshold (FT) expansion of the FvK equations (16).

The next order in the FT expansion, as described in *Supporting Information*, yields corrections to the stress tensor at $O(f^1)$; these corrections arise as the price of avoiding a large, energetically costly shear stress $|\sigma_{xy}| \sim |\zeta_0'(x)(f/\lambda)| = O(1)$. In particular, we find a correction to the stress along the wrinkles' direction

$$\sigma_{xx}^{(1)} = -Y\zeta_0''(x)f\cos(2\pi y/\lambda), \qquad [7]$$

which exists only if the mean shape, $\zeta_0(x)$, is curved in the wrinkles' direction. The significance of the correction in [7] can be understood by substituting this stress component into the first FvK equation [3], where it gives rise to a new force that is proportional to f: an entirely new source of stiffness.

In detail, the linearized normal force balance [3] reads

$$\left[B\left(\frac{2\pi}{\lambda}\right)^4 - T\frac{d^2}{dx^2} + Y\zeta_0''^2 + K_{\text{sub}}\right]f = -\sigma_{yy}\left(\frac{2\pi}{\lambda}\right)^2 f, \qquad [8]$$

which, together with Eq. **5**, admits a solution for any λ. Inspection of Eq. **8** reveals the mechanism underlying wrinkle formation. As in Euler buckling, a destabilizing compressive force ($\sim \sigma_{yy}$) is resisted by a stabilizing bending force ($\sim B$), which favors small curvature (large λ). However, Eq. **8** reveals three other types of stabilizing forces: the tension along wrinkles ($\sim T$), the stiffness of the substrate ($\sim K_{\text{sub}}$), and its curvature along the wrinkle direction ($\sim \zeta_0''$), all of which favor small-amplitude wrinkles (hence small λ, by [5]). This competition leads to the wavelength selection expressed in Eq. **1**.

We define the energy density $\mathcal{H}_0[\lambda]$ of wrinkles with wavelength λ by identifying the leading terms of the energy associated with the restoring forces in [8], and using Eq. **5**,

$$\mathcal{H}_0[\lambda] = \Phi(x)^2\left\{\frac{B}{2}(2\pi)^4\big/\lambda^2 + \frac{\lambda^2}{2}K_{\text{eff}}(x)\right\}, \qquad [9]$$

where the effective stiffness K_{eff}, given by Eq. **2**, was obtained by replacing the relevant tension-field terms in Eq. **8** [namely, the $O(f^0)$ part of the FT expansion] by their local values at x; namely, $T \to \sigma_{\parallel}(x)$; $(\zeta_0'')^2 \to R_{\parallel}(x)^{-2}$. Here, $\sigma_{\parallel}(x), R_{\parallel}(x)^{-1}$ are the local values of the components of the stress and curvature tensors along the wrinkle direction. Minimizing $\mathcal{H}_0[\lambda]$, we obtain Eq. **2**. Importantly, this derivation assumes that the wavelength varies sufficiently slowly in space so that the energetic cost of gradients in the wavelength, $d\lambda/dx$ [due to the stress induced by spatial changes in the wrinkle number (17, 18)] is negligible compared with $\mathcal{H}_0[\lambda]$. Later on, we discuss a more complete framework that does not make this assumption. Minimizing the local wrinkle energy density $\mathcal{H}_0[\lambda(x)]$ everywhere, we obtain the local λ law, Eqs. **1** and **2**.

Following ref. 1, we note that the three terms that compose K_{eff}, Eq. **2**, correspond to distinct types of stiffness, associated with the substrate, the exerted tension, and the curvature along the wrinkles. By analogy to the substrate stiffness K_{sub}, we call the last two terms, respectively, a tension-induced stiffness (K_{tens}) and a curvature-induced stiffness (K_{curv}). [We note two subtleties of the setup shown in Fig. 1*B* that are not discussed in ref. 1. First, the tension-induced stiffness, K_{tens}, operates only when the confinement varies spatially, namely, $\Phi = \Phi(x)$. Second, our experience with this experimental geometry suggests that the occurrence and extent of wrinkles are very sensitive to gradients created at the boundary.] Notably, the curvature-induced stiffness has no explicit dependence on any force. Instead, it reflects the sheet's elastic response to the curved geometry alone. To our knowledge, the geometric stiffness of sheets, which resembles a

shell's resistance (19), has not been noted before. We will show that it can have a dramatic effect on the wrinkle's wavelength.

Before proceeding to discuss specific examples, let us note that although the tension-induced stiffness K_{tens} may be negligible in comparison with K_{sub} or K_{curv}, wrinkle patterns that are described by a local λ law are often characterized by the existence of a tensile direction ($\sigma_\parallel(x) \gg |\sigma_\perp(x)|$), whose spatial variation occurs over a much larger scale than λ. Although Eq. 1 may be relevant also for more complex types of wrinkle patterns [e.g., under biaxial compression (20) or depressurizing a shell with a stiff core (21)], confinement of sheets in the absence of an imposed tension often leads to patterns with deep folds or stress-focusing zones (22–24), rather than to the oscillatory wrinkles described by Eqs. 1 and 2 and manifested in the following experimental examples.

Indentation of a Floating Sheet

To test the local λ law, we study the indentation of a thin polystyrene (PS) sheet (thickness 40 nm $< t <$ 400 nm) floating on a deionized water bath. The sheet has Young's modulus $E = 3.4$ GPa and Poisson's ratio $\Lambda = 0.34$, and the bath has surface tension $\gamma = 72$ mN/m and density 1,000 kg/m^3. The sheet is poked from beneath by a rod with a spherical tip of radius 0.79 mm. The deformation is observed by two cameras that capture the side and top views of the sheet. The indentation height δ is changed by a translation stage and is measured with an accuracy of 50 μm.

The combination of loads due to the indentation height δ at the center ($r = 0$), the liquid–vapor surface tension γ that pulls the edge of the sheet ($r = R_{film}$), and the liquid gravity ρg leads to azimuthal compression that is released by radial wrinkles (Fig. 2 A–D). In ref. 11, tension-field theory was used to predict the macroscale axially symmetric shape $\zeta_0(r)$. (There, the sheet was poked from above, but the same predictions apply here, because the gravitational potential energy of the liquid is quadratic in ζ.) The wrinkle pattern is governed by the dimensionless indentation height, $\widetilde{\delta} = \sqrt{Y/\gamma} \cdot (\delta/\ell_c)$, where $\ell_c = \sqrt{\gamma/\rho g}$ is the capillary length. For sufficiently large δ, wrinkles cover the whole sheet (except in a small tensile core at the center), and the tension-field prediction for the shape $\zeta_0(r)$ becomes $\zeta_0(r) \approx \delta \mathrm{Ai}(r/\ell_{curv})/\mathrm{Ai}(0)$, where $\ell_{curv} = R_{film}^{1/3}\ell_c^{2/3}$, and $\mathrm{Ai}(x)$ is the Airy function (11). Our measurements of the radial profile show excellent agreement with this prediction, for a wide range of thickness t and a factor of 2 in R_{film}, as shown in Fig. 2 E and F. The sheet returns to being flat over the scale ℓ_{curv}, as predicted.

The shape $\zeta_0(r)$ predicted in ref. 11 allows us to compute the curvature $R_\parallel(r)^{-1} \approx \zeta_0''$ along the wrinkles and hence the curvature-induced stiffness $K_{curv}(r) = Y/R_\parallel^2$. Furthermore, the tension-field calculation also yields the stress $\sigma_\parallel(r) \approx \gamma R_{film}/r$ and thence the value of $\Phi = (\pi r/\lambda) f$ in this polar geometry, from which we compute the tension-induced stiffness $K_{tens}(r) = \sigma_\parallel|\Phi'/\Phi|^2$ (details in *Supporting Information*). These stiffnesses, together with $K_{sub} = \rho g$ due to the liquid gravity, yield predictions for the wrinkle wavelength, via Eqs. 1 and 2.

For $\widetilde{\delta} \gtrsim 15$, theory predicts that $K_{curv}(r) \gg K_{tens}(r), K_{sub}$ in most of the wrinkled zone. Hence, Eq. 1 yields

$$\lambda(r) \approx 2\pi\left(BR_\parallel(r)^2/Y\right)^{1/4} = Z(r) \cdot \sqrt{t/\delta}, \qquad [10]$$

where $Z(r) = 2\pi\sqrt{\mathrm{Ai}(0)}/[12(1-\Lambda^2)]^{1/4}(\ell_{curv}^3/r\mathrm{Ai}(r/\ell_{curv}))^{1/2}$ is independent of t. Fig. 3A shows the experimentally measured wrinkle wavelength at a fixed radial distance $r = \ell_{curv}$ (safely in the middle of the wrinkled zone), as a function of indentation height, for a wide range of sheet thickness. For $\widetilde{\delta} \gtrsim 15$, Fig. 3B shows not only a collapse of the data with the predicted (curvature-dominated) scaling relation, $\lambda(r = \ell_{curv}) \sim \sqrt{t/\delta}$, but also a quantitative agreement with the predicted t-independent prefactor $Z(r)$ in Eq. 10.

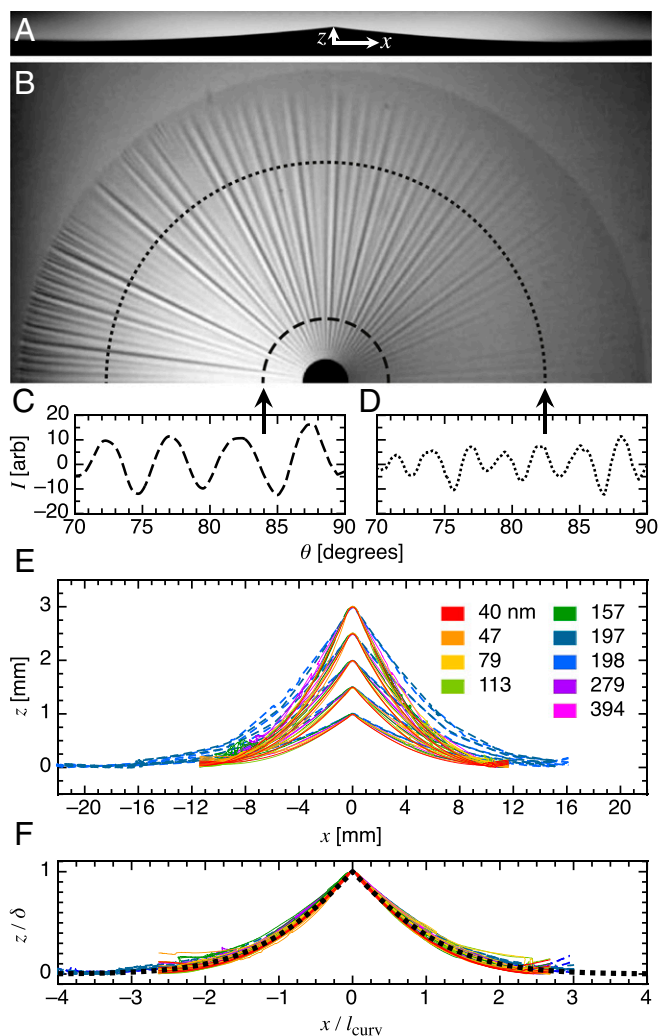**Fig. 2.** Axisymmetric deformations of an indented polymer film. (*A* and *B*) Side and top views of a polystyrene (PS) film of thickness $t = 113$ nm and radius $R_{film} = 11.1$ mm, floating on water and indented to height $\delta = 0.59$ mm at its center. A pattern of radial wrinkles emerges. (*C* and *D*) Filtered image intensity, I, vs. polar angle θ at radii $r = 0.2R_{film}$ and $r = 0.7R_{film}$. Within an angular sector (here, 20° wide) there are more wrinkles at the larger radius. Thus, the wrinkle number, $m(r) = 2\pi r/\lambda(r)$, varies spatially. (*E*) Side profiles: height of sheet, z, vs. horizontal coordinate, x. The $t = 197$-nm sheet corresponds to $R_{film} = 17.5$ mm, and $t = 198$ nm corresponds to $R_{film} = 22.2$ mm; the rest have $R_{film} = 11.1$ mm. (The z scale is stretched to show detail.) (*F*) The same data scaled by δ and ℓ_{curv}. The data over a wide range of thicknesses, radii, and poking amplitudes all follow the predicted Airy function shape (dotted curve).

For smaller values of indentation height, the data deviate from curvature-dominated behavior. This is in agreement with the local λ law, which predicts that K_{tens} becomes appreciable here as shown by the solid black curves in Fig. 3B that include all three terms in K_{eff} (and exhibit also a weak dependence on sheet size through R_{film}/ℓ_c).

In Fig. 4 we plot the number of wrinkles, $m(r) = 2\pi r/\lambda(r)$. [Plotting $m(r)$, rather than $\lambda(r)$, emphasizes that the number of wrinkles changes with radial distance r.] Results are shown for a wide range of t and $\widetilde{\delta}$ and for two film radii: $R_{film} = 11.1$ cm (Fig. 4 *A* and *B*) and $R_{film} = 22.2$ cm (Fig. 4*C*). The colored curves show the prediction from Eqs. 1 and 2, whereas the black curve is obtained by approximating $K_{eff} \approx K_{curv}$ and is valid only if $K_{curv} \gg K_{tens}, K_{sub}$.

As we saw in Fig. 3, K_{curv} dominates the other stiffnesses (K_{tens} and K_{sub}) for $r \sim \ell_{curv}$; here we see that K_{curv} is dominant also for
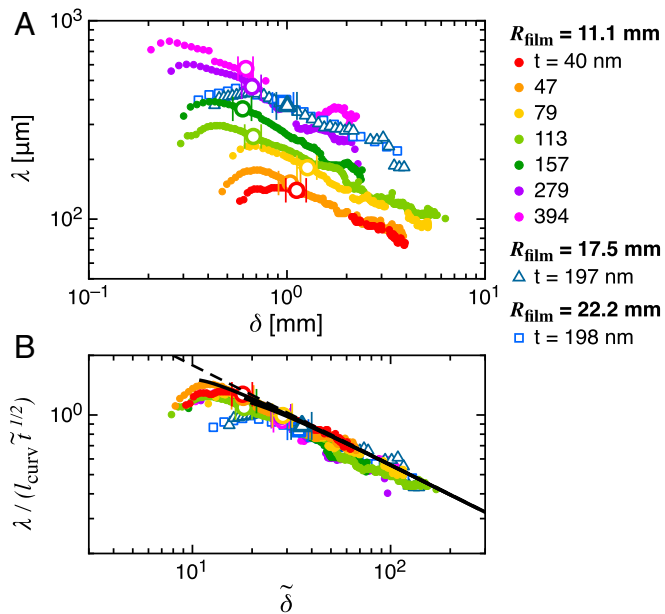
Fig. 3. Effects of geometry and tension on the wrinkle pattern. (*A*) Wrinkle wavelength, λ (measured at $r = \ell_{curv}$) vs. indentation amplitude, δ, for a floating PS sheet. Solid circles: $R_{film} = 11.1$ mm. Open triangles: $R_{film} = 17.5$ mm. Open squares: $R_{film} = 22.2$ mm. For each thickness, wavelength is measured from wrinkle onset as δ is slowly increased. The appearance of crumples is denoted by the large open symbols, beyond which wavelength is measured in an angular sector between two crumples. (*B*) The data are collapsed using rescaled variables, $\lambda/(\ell_{curv}\tilde{t}^{1/2})$ and $\tilde{\delta}$, where the tilde denotes scaling by $\ell_c\sqrt{\gamma/Y}$. Solid curves: theoretical prediction with all three stiffnesses (upper and lower solid curves, distinguishable only by their starting points, are for $R_{film} = 11.1$ mm and $R_{film} = 22.2$ mm, respectively). Dashed line: theoretical prediction with just the geometric stiffness term, $K_{eff} \approx K_{curv}(r = \ell_{curv})$, $\lambda/(\ell_{curv}\tilde{t}^{1/2}) \approx 5.64\tilde{\delta}^{-1/2}$.

consequently a linear variation of m with radial distance (26):
$$m(r) \cdot \sqrt{t/\delta} = [12(1 - \Lambda^2)]^{1/4} (\tilde{\delta}^{1/2}\ell_c)^{-1} \cdot r.$$

Approaching the edge of the film, there is a substantial increase in $m(r)$ [decrease in $\lambda(r)$]. Such a "wrinkling cascade" was observed in experiments on a flat liquid bath, where the wrinkle amplitude is suppressed at the edge of the film by a liquid meniscus, and the cascade was shown to decay over a distance $\sim\ell_c$ from the edge (27). Our experiments show a strong, as yet unexplained dependence of the decay length on the indentation height (Fig. 4*B*). (Fig. 4*C* presents data from large sheets; here the edge fell outside the illuminated region, so the edge cascade was not visible). The local effect of the liquid meniscus or other boundary forces (18, 28–30) are not accounted for in Eqs. **1** and **2**.

Finally, Figs. 3 and 4 also include data at large values of the indentation height where crumples and folds appear in the sheet. In contrast to the purely wrinkled state where the shape undulates around an axially symmetric profile $\zeta_0(r)$, the folded state consists of a polygonal shape decorated by wrinkles (23). The excellent agreement with our prediction of $\lambda(r)$, which assumes an axisymmetric profile $\zeta_0(r)$, indicates that between adjacent folds, the height profile closely follows the axisymmetric prediction (i.e., the Airy function shown in Fig. 2*F*). This surprising observation echoes recent studies on a related system (24).

A Sheet on a Drop

To test the generality of the local λ law, we study wrinkling of a circular PS sheet in another geometry: a liquid surface with positive Gaussian curvature. This is experimentally realized by placing the sheet on (*i*) an air–water meniscus (as in ref. 8) or (*ii*) a water drop in oil (dodecane or silicone oil) (24) and controlling the curvature R of the water meniscus.

The dimensionless confinement, $\alpha = YR_{film}^2/(2\gamma R^2)$, plays a similar role (8) to that of the dimensionless amplitude δ in the indentation setup. This parameter expresses the ratio between tensional terms and the Laplace pressure, $P = 2\gamma/R$, which acts normal to the sheet. For $\alpha \gtrsim 5.16$, radial wrinkles form in the outer part of the sheet to relax azimuthal compression (8), as pictured in Fig. 5*A*. The wrinkled zone grows as α increases. In Fig. 5 *B* and *C*, *Insets* show the number of wrinkles, $m(r)$, for several thicknesses and values of α.

A tension-field solution to the FvK equation was found (8), using the assumption of small slopes, valid for $R_{film} \ll R$. This yields all of the quantities needed to evaluate the stiffness: the

other r as the indentation increases. Close to the inner boundary of the wrinkled zone, the tension-induced stiffness, K_{tens}, has a strong effect [due to the divergence of $\Phi'(r)$ (25)] within a region that becomes narrower as δ increases. For larger r, the wrinkled sheet is almost planar, and the dominant stiffness is due to the substrate; we then expect $\lambda(r) = 2\pi(B/\rho g)^{1/4} = \text{cst}$ and
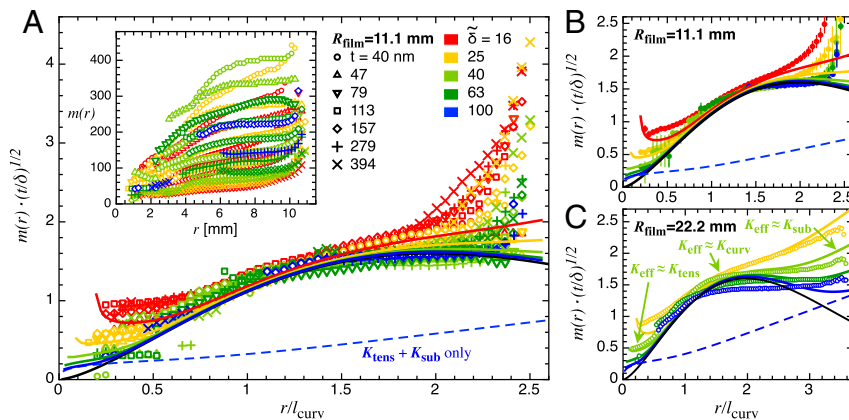
Fig. 4. Spatial variation of wrinkles for an indented, floating PS sheet. (*A*, *Inset*) Wrinkle number, m, vs. radial coordinate, r. Sheet thickness (indicated by symbol shape) and indentation amplitude (indicated by color) are both varied. In *A*, the data collapse in the rescaled variables, $m(r) \cdot (t/\delta)^{1/2}$ and r/ℓ_{curv}, following separate curves for each value of $\tilde{\delta}$. As indentation increases, the data approach the theoretical prediction evaluated in the limit of large $\tilde{\delta}$ (solid black curve). Solid colored curves: Theoretical predictions including the stretching and gravity terms, which become significant at small and large radii, respectively, for finite $\tilde{\delta}$. If the curvature term is omitted, the result does not describe the data (blue dashed curve calculated for *A*–*C* at $\tilde{\delta} = 100$). (*B*) Averages over sheet thickness at each value of $\tilde{\delta}$. (The edge of the film is at $R_{film}/\ell_{curv} = 2.56$.) (*C*) Results for a larger sheet: $R_{film} = 22.2$ mm, $t = 198$ nm. For large r/ℓ_{curv}, the gravity term becomes dominant over the curvature term, causing m to rise. (The edge of the film is at $R_{film}/\ell_{curv} = 4.06$.)

Fig. 5. Spatial variation of wrinkles for a sheet on a drop. (*A*) Top view of a circular PS sheet of thickness 77 nm and radi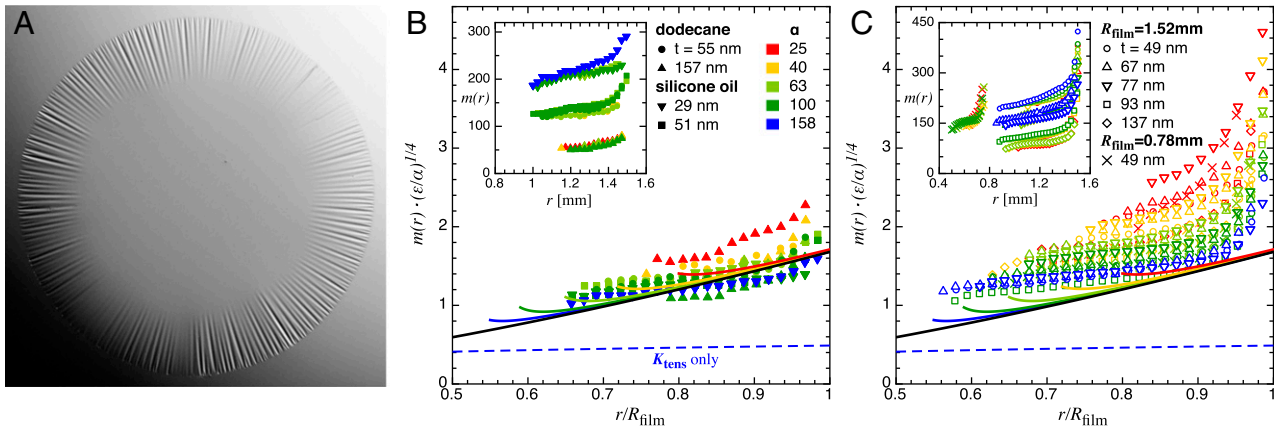us $R_{film} = 1.52$ mm at a curved air–water meniscus (here $\alpha = 97$). Radial wrinkles extend from the edge of the sheet inward. (*B, Inset*) Spatial variation of wrinkle number, $m(r)$, for a circular sheet of radius $R_{film} = 1.52$ mm on an axisymmetrically curved meniscus (a water drop immersed in oil). The drop was formed in a glass container filled with either dodecane or silicone oil, sitting on a layer of fluorinated oil, as in ref. 24. The curvature was controlled by withdrawing fluid from the drop through a needle. Sheet thickness was also varied. Interfacial tension was measured by analyzing the gravitational deformation of the liquid interface away from the sheet and ranged from $\gamma = 19.0$ mN/m to 32.5 mN/m. In *B*, the data are collapsed using rescaled variables, $m(r) \cdot (\epsilon/\alpha)^{1/4}$ and r/R_{film}. Solid colored curves: Theoretical predictions with curvature and stretching terms. As confinement increases, the curves approach the theoretical prediction with $K_{eff} \approx K_{curv}$, indicating that curvature underlies the dominant substrate stiffness (black curve). Dashed curve: Prediction with only the stretching term ($K_{eff} \approx K_{tens}$), calculated at $\alpha = 158$. (*C*) Corresponding measurements for a sheet at an air–water interface ($\gamma = 72$ mN/m), formed at the end of a cylindrical tube (sheet radius and thickness denoted in *Inset*). The curvature was controlled by varying the hydrostatic pressure (8).

radial profile $\zeta_0(r; \alpha)$, the radius of the tensile (unwrinkled) core, the radial (tensile) stress component $\sigma_{rr} = \gamma R_{film}/r$, and the absorbed length $\sim \Phi(r; \alpha)^2 = m^2 f(r)^2$.

In our experiments, the substrate stiffness due to the gravity of the drop is negligible because the sheet's radius (and the deformation of liquid it induces) is smaller than the capillary length. Hence, according to Eqs. **1** and **2**, the wavelength $\lambda(r)$ is determined only by the tension-induced and curvature-induced stiffnesses. As α increases, K_{curv} becomes significantly larger than K_{tens}. To illustrate this point, the predictions for the number of wrinkles based on K_{tens} alone (dashed blue curve) and K_{curv} alone (solid black curve) are shown in Fig. 5. Hence one may predict $m(r)$ using the local λ law with $K_{eff} \approx K_{curv}$ and $\zeta_0'' \approx 2r/(RR_{film})$ (8) to give

$$m(r) = 2\pi r/\lambda(r) \approx (8\alpha/\epsilon)^{1/4} (r/R_{film})^{3/2}, \qquad \textbf{[11]}$$

where the bendability, $\epsilon^{-1} = \gamma R_{film}^2/B$ (16). As in indentation, K_{curv} becomes ever more dominant as confinement increases.

Fig. 5 shows our measurements of $m(r)$ for a range of thicknesses, 20 nm $< t <$ 160 nm, and confinement values, $20 < \alpha < 160$. The quantitative agreement between the data and the prediction of the local λ law, Eqs. **1** and **2**, with no fitting parameters, is especially good at large values of the confinement α in Fig. 5*B*. Fig. 5*C* shows quantitative deviations from the prediction, which may be due to the liquid meniscus at the free edge of the sheet; surface tension is larger in Fig. 5*C* than in Fig. 5*B*, as denoted in the figure legend. The wrinkling cascade due to the liquid meniscus, which causes $m(r)$ to rise at the edge of the sheet, is not accounted for in the predictions we are testing. We note that the cascade occupies a region that is much shorter than the capillary length ($\ell_c = 2.7$ mm for the data in Fig. 5*C*). These observations, along with what was noted in the previous section for indentation, suggest that the boundary cascade may be more complicated in curved geometries than in a flat geometry, where the cascade dies exponentially with a penetration length $\sim \ell_c$ from the free edge (27).

Another common feature between this geometry and the indentation experiment is an instability at a finite, large value of the relevant confinement parameter (δ or α) in which the sheet becomes decorated with crumples (8). Nonetheless, the above prediction for the number of wrinkles $m(r)$, which assumes the

radial curvature of the axisymmetric state, still agrees with the data beyond this transition ($\alpha \gtrsim 150$).

Discussion

We have shown excellent agreement between the prediction of the local λ law, Eqs. **1** and **2**, and experimental measurements of the spatially varying wrinkle wavelength in two different geometries: one with negative and one with positive Gaussian curvature. This agreement illustrates the key role played by the geometric stiffness, K_{curv}, and provides strong evidence for the validity of the local λ law in relatively complex scenarios.

A similar type of geometric stiffness, which is determined by the underlying curvature rather than by the exerted loads, is known to govern the (unwrinkled) response of intrinsically curved elastic shells to loads (19). To demonstrate the geometric link between shells and sheets, consider the uniaxial compression of a cylindrical shell: An ordered pattern of diamond-like blocks is observed (31), whose characteristic size is proportional to the geometric mean of the radius (R) and thickness (t) of the shell, $\lambda \propto \sqrt{tR}$. This result may be obtained simply from Eq. **1** by substituting $K_{eff} = K_{curv} = Y/R^2$. A similar intermediate scale characterizes the formation of dimples in a depressurized shell (21, 32). This observation suggests that the calculation of K_{curv} that was performed here for the one-dimensional wrinkling ansatz (4) may extend to other, more complex patterns, including those observed, e.g., in ref. 31. To our knowledge, Eqs. **1** and **2** compose the first attempt to describe the combined effect of the geometric stiffness, K_{curv}, with the more familiar, mechanical sources of stiffnesses, K_{sub} and K_{tens}, and thus provide a quantitative platform for predicting the microscale features of wrinkle patterns.

Notwithstanding the experimental evidence for the local λ law, Eqs. **1** and **2**, its validity is limited to situations in which the spatial variation of the wavelength $\lambda(x)$ across the wrinkled sheet is sufficiently slow. In the Ginzburg–Landau terminology, we expect that $\lambda(x)$ is obtained as the minimizer of a more general, effective "coarse-grained" energy functional:

$$\mathcal{H}_0[\lambda] + \mathcal{H}_1[\nabla(a(x)\lambda)]. \qquad \textbf{[12]}$$

In this article we have accounted only for $\mathcal{H}_0$, given by Eq. **9**. Going beyond this, one might expect situations in which gradients

in the wrinkle wavelength are explicitly penalized via $\mathcal{H}_1$, with $a(x)$ accounting for deviations of the wrinkle direction from the tension lines spanned by the principal direction of the stress tensor. For example, in the cylindrical geometry of Fig. 1*C*, the tension lines are parallel to $(\mathbf{e}_x)$ so that $a(x) = \text{cst}$. In the axisymmetric setups studied here, the tension lines are radial, so deviations of $m(r) = 2\pi r/\lambda(r)$ from a constant value require some stretching. We therefore expect that $a(r) \propto 1/r$. Thus, $\mathcal{H}_1$ encapsulates bending and splaying of wrinkles beyond those prescribed by the asymptotic stress field through $a(x)$. The specific form of $\mathcal{H}_1$ remains unknown, despite some recent works that addressed the energetic cost associated with smooth and sharp transformations of n wrinkles to $n + m$ wrinkles (17, 18, 25). However, the unexpectedly good agreement obtained between the simple local λ law and experiments suggests that, in circumstances that remain to be understood, the effect of $\mathcal{H}_1$ may safely be neglected.

Materials and Methods

Film Preparation. We made polymer films by spin-coating dilute solutions of polystyrene ($M_n = 91$ kDa, $M_w = 95$ kDa or $M_n = 99$ kDa, $M_w = 105.5$ kDa; Polymer Source, Inc.) in toluene onto glass microscope slides, following ref. 5.

Different thicknesses were produced by varying the spinning speed (800–4,000 rpm) or the polymer concentration (1–5% by weight). Film thickness was measured with a white-light interferometer (Filmetrics F20-UV). Circular films were cut from the center of the slides, where thickness was found to be uniform to within 2%.

Wrinkle Analysis. We performed a custom automated analysis (adapted from ref. 8) of the top-view images to measure wavelength, λ, as a function of radial coordinate in the wrinkle patterns. To reduce noise, image intensity was first averaged over small intervals along the radial coordinate. We then filtered the signal in the θ coordinate, to eliminate long-wavelength components due to uneven lighting. Finally, an autocorrelation was performed at each radius, which gave a decaying sinusoidal signal. The wrinkle wavelength was determined as twice the distance to the first autocorrelation trough. When crumples or folds were present, angular sectors lying between these structures were analyzed in the same fashion.

1. Cerda E, Mahadevan L (2003) Geometry and physics of wrinkling. *Phys Rev Lett* 90(7): 074302.
2. Genzer J, Groenewold J (2006) Soft matter with hard skin: From skin wrinkles to templating and material characterization. *Soft Matter* 2:310–323.
3. Breid D, Crosby AJ (2011) Effect of stress state on wrinkle morphology. *Soft Matter* 7: 4490–4496.
4. Stafford CM, et al. (2004) A buckling-based metrology for measuring the elastic moduli of polymeric thin films. *Nat Mater* 3(8):545–550.
5. Huang J, et al. (2007) Capillary wrinkling of floating thin polymer films. *Science* 317(5838):650–653.
6. Schroll RD, et al. (2013) Capillary deformations of bendable films. *Phys Rev Lett* 111(1): 014301.
7. Burton K, Taylor DL (1997) Traction forces of cytokinesis measured with optically modified elastic substrata. *Nature* 385(6615):450–454.
8. King H, Schroll RD, Davidovitch B, Menon N (2012) Elastic sheet on a liquid drop reveals wrinkling and crumpling as distinct symmetry-breaking instabilities. *Proc Natl Acad Sci USA* 109(25):9716–9720.
9. Grason GM, Davidovitch B (2013) Universal collapse of stress and wrinkle-to-scar transition in spherically confined crystalline sheets. *Proc Natl Acad Sci USA* 110(32): 12893–12898.
10. Hohlfeld E, Davidovitch B (2015) Sheet on a deformable sphere: Wrinkle patterns suppress curvature-induced delamination. *Phys Rev E Stat Nonlin Soft Matter Phys* 91(1):012407.
11. Vella D, Huang J, Menon N, Russell TP, Davidovitch B (2015) Indentation of ultrathin elastic films and the emergence of asymptotic isometry. *Phys Rev Lett* 114(1):014301.
12. Stein M, Hedgepeth JM (1961) *Analysis of Partly Wrinkled Membranes* (Natl Aeronautics Space Admin, Washington) Technical Note D-813.
13. Mansfield EH (1989) *The Bending and Stretching of Plates* (Cambridge Univ Press, Cambridge, UK).
14. Pipkin AC (1986) The relaxed energy density for isotropic elastic membranes. *IMA J Appl Math* 36(1):85–99.
15. Steigmann DJ (1990) Tension-field theory. *Proc R Soc Lond A Math Phys Sci* 429(1876): 141–173.
16. Davidovitch B, Schroll RD, Vella D, Adda-Bedia M, Cerda EA (2011) Prototypical model for tensional wrinkling in thin sheets. *Proc Natl Acad Sci USA* 108(45):18227–18232.

17. Davidovitch B (2009) Period fissioning and other instabilities of stressed elastic membranes. *Phys Rev E Stat Nonlin Soft Matter Phys* 80(2 Pt 2):025202.
18. Vandeparre H, et al. (2011) Wrinkling hierarchy in constrained thin sheets from suspended graphene to curtains. *Phys Rev Lett* 106(22):224301.
19. Vella D, Ajdari A, Vaziri A, Boudaoud A (2012) The indentation of pressurized elastic shells: From polymeric capsules to yeast cells. *J R Soc Interface* 9(68):448–455.
20. Kohn RV, Nguyen HM (2013) Analysis of a compressed thin film bonded to a compliant substrate: The energy scaling law. *J Nonlinear Sci* 23:343–362.
21. Stoop N, Lagrange R, Terwagne D, Reis PM, Dunkel J (2015) Curvature-induced symmetry breaking determines elastic surface patterns. *Nat Mater* 14(3):337–342.
22. Chopin J, Kudrolli A (2013) Helicoids, wrinkles, and loops in twisted ribbons. *Phys Rev Lett* 111(17):174302.
23. Holmes DP, Crosby AJ (2010) Draping films: A wrinkle to fold transition. *Phys Rev Lett* 105(3):038303.
24. Paulsen JD, et al. (2015) Optimal wrapping of liquid droplets with ultrathin sheets. *Nat Mater* 14(12):1206–1209.
25. Bella P, Kohn R (2014) Wrinkles as the result of compressive stresses in an annular thin film. *Commun Pure Appl Math* 67:693–747.
26. Piñeirua M, Tanaka N, Roman B, Bico J (2013) Capillary buckling of a floating annulus. *Soft Matter* 9:10985–10992.
27. Huang J, Davidovitch B, Santangelo CD, Russell TP, Menon N (2010) Smooth cascade of wrinkles at the edge of a floating elastic film. *Phys Rev Lett* 105(3):038302.
28. Pomeau Y (1998) Buckling of thin plates in the weakly and strongly nonlinear regimes. *Philos Mag B* 78:235–242.
29. Belgacem HB, Conti S, DeSimone A, Muller S (2000) Rigorous bounds for the Foppl-von Karman theory of isotropically compressed plates. *J Nonlinear Sci* 10:661–683.
30. Jin W, Sternberg P (2001) Energy estimates for the von Karman model of thin-film blistering. *J Math Phys* 42(1):192–199.
31. Tennyson R (1964) Buckling of circular cylindrical shells in axial compression. *AIAA J* 2: 1351–1353.
32. Hutchinson JW (1967) Imperfection sensitivity of externally pressurized spherical shells. *J Appl Mech* 34(1):49–55.
33. Cerda E, Ravi-Chandar K, Mahadevan L (2002) Thin films. Wrinkling of an elastic sheet under tension. *Nature* 419(6907):579–580.

APPLIED PHYSICAL SCIENCES